



Title	Characteristic alpha and He-6 decays of linear-chain structures in C-16
Author(s)	Baba, Tomoyuki; Kimura, Masaaki
Citation	Physical Review C, 97(5), 054315 <a href="https://doi.org/10.1103/PhysRevC.97.054315">https://doi.org/10.1103/PhysRevC.97.054315</a>
Issue Date	2018-05-14
Doc URL	<a href="http://hdl.handle.net/2115/71439">http://hdl.handle.net/2115/71439</a>
Rights	©2018 American Physical Society
Rights(URL)	<a href="https://creativecommons.org/licenses/by/4.0/">https://creativecommons.org/licenses/by/4.0/</a>
Type	article
File Information	PhysRevC.97.054315.pdf



[Instructions for use](#)

# Characteristic $\alpha$ and ${}^6\text{He}$ decays of linear-chain structures in ${}^{16}\text{C}$

T. Baba<sup>1</sup> and M. Kimura<sup>1,2</sup><sup>1</sup>*Department of Physics, Hokkaido University, 060-0810 Sapporo, Japan*<sup>2</sup>*Reaction Nuclear Data Centre, Faculty of Science, Hokkaido University, 060-0810 Sapporo, Japan*

(Received 15 January 2018; published 14 May 2018)

The linear-chain states of  ${}^{16}\text{C}$  and their decay modes are theoretically investigated by using the antisymmetrized molecular dynamics. It is found that the positive-parity linear-chain states have the  $(3/2_{\pi}^{-})^2(1/2_{\sigma}^{-})^2$  configuration and primary decay to  ${}^{12}\text{Be}(2_1^+)$  as well as to  ${}^{12}\text{Be}(\text{g.s.})$  by  $\alpha$ -particle emission. Moreover, we show that they also decay via the  ${}^6\text{He} + {}^{10}\text{Be}$  channel. In the negative-parity states, it is found that two types of linear chains exist. One has the valence neutrons occupying the molecular orbits  $(3/2_{\pi}^{-})^2(1/2_{\sigma}^{-})(3/2_{\pi}^+)$ , while the other's configuration cannot be explained in terms of the molecular orbits because of the strong parity mixing. Both configurations constitute the rotational bands with a large moment of inertia and intraband  $E2$  transitions. Their  $\alpha$  and  ${}^6\text{He}$  reduced widths are sufficiently large to be distinguished from other noncluster states although they are smaller than those of the positive-parity linear chain.

DOI: [10.1103/PhysRevC.97.054315](https://doi.org/10.1103/PhysRevC.97.054315)

## I. INTRODUCTION

Recent years have seen many important experimental and theoretical studies for the linear-chain states (linearly aligned  $3\alpha$  particles) in  ${}^{14}\text{C}$  [1–16] and  ${}^{16}\text{C}$  [17–23]. In these C isotopes several theoretical studies have predicted the existence of linear-chain states with the valence neutrons playing a glue-like role to stabilize the extreme shape. Antisymmetrized molecular dynamics (AMD) calculations for  ${}^{14}\text{C}$  [5,11,15] predict a positive-parity rotational band with the linear-chain configuration having the  $\pi$ -bond valence neutrons. The calculations also suggest a unique decay pattern of the  $\pi$ -bond linear chain, i.e., it decays not only to the  ${}^{10}\text{Be}(0_1^+)$  but also to the  ${}^{10}\text{Be}(2_1^+)$  by the  $\alpha$ -particle emission. The energies, moment of inertia, and decay pattern of the resonances observed by the  $\alpha + {}^{10}\text{Be}$  elastic scattering [7,9,13] reasonably agree with the predicted  $\pi$ -bond linear chain. Therefore, the  $\pi$ -bond linear-chain formation in  ${}^{14}\text{C}$  looks assured. In addition to the  $\pi$ -bond linear chain, we also predict another linear chain which has  $\sigma$ -bond neutrons. This band should have a different decay pattern because it will dominantly decay to  ${}^{10}\text{Be}(0_2^+)$  and  ${}^{10}\text{Be}(2_3^+)$ . Although experimental evidence is still lacking, the resonances observed by the  ${}^9\text{Be}({}^9\text{Be}, \alpha + {}^{10}\text{Be})\alpha$  reaction [14] looks promising as candidates for the  $\sigma$ -bond linear chain.

The advances in the study of  ${}^{14}\text{C}$  naturally motivate us to study the linear chains in neutron-rich C isotopes. In particular, we expect that linear-chain states should also exist in  ${}^{16}\text{C}$  [22] because both  $\pi$ - and  $\sigma$ -bonding orbits are simultaneously occupied by valence neutrons. The molecular-orbital model calculation [17] predicted that  ${}^{16}\text{C}$  has in fact the most substantial linear chain among the C isotopes. Furthermore, our previous work [22] predicted a positive-parity linear-chain band built on the  $0^+$  state at 15.5 MeV, which should be verified experimentally. In this work, for further experimental study, we provide additional theoretical information. The first is negative-parity states. In the case of  ${}^{14}\text{C}$ , experiments have reported the negative-parity resonances [7,9,13]. Therefore,

theoretical predictions are also needed for the negative-parity resonances in  ${}^{16}\text{C}$ . The second is the decay mode of the linear-chain configuration. Because the linear-chain band of  ${}^{16}\text{C}$  is predicted above the  $\alpha + {}^{12}\text{Be}$  and  ${}^6\text{He} + {}^{10}\text{Be}$  thresholds, the decay pattern should provide important information to identify the linear chain.

In this work, based on AMD calculations, we study the positive- and negative-parity linear-chain states of  ${}^{16}\text{C}$  and discuss their decay patterns. The positive-parity linear chain has the valence neutrons occupying molecular orbits  $(3/2_{\pi}^{-})^2(1/2_{\sigma}^{-})^2$ . We predict that the linear-chain states primarily decay to  ${}^{12}\text{Be}(2_1^+)$  as well as to  ${}^{12}\text{Be}(\text{g.s.})$ . They will also decay to  ${}^{10}\text{Be}(\text{g.s.})$  and  ${}^{10}\text{Be}(2_1^+)$  by  ${}^6\text{He}$  emission, which is a signature of the covalency of valence neutrons.

In the negative parity, two rotational bands composed of the linear-chain configuration are found. One has the valence neutrons occupying the molecular orbits  $(3/2_{\pi}^{-})^2(1/2_{\sigma}^{-})(3/2_{\pi}^+)$ , and the other does not have a clear molecular-orbit configuration. Their  $\alpha$  and  ${}^6\text{He}$  reduced widths are smaller than those of the positive-parity linear-chain band, but sufficiently large to be distinguished from other noncluster states.

The paper is organized as follows: The AMD framework is briefly explained in the next section. In Sec. III, the density distribution on the energy surface, excitation energies, and decay widths are discussed for positive and negative parity. In the last section, we summarize this work.

## II. THEORETICAL FRAMEWORK

### A. Variational calculation and generator coordinate method

The microscopic  $A$ -body Hamiltonian used in this work reads

$$\hat{H} = \sum_{i=1}^A \hat{t}_i - \hat{t}_{\text{c.m.}} + \sum_{i<j}^A \hat{v}_{ij}^N + \sum_{i<j}^Z \hat{v}_{ij}^C, \quad (1)$$

where Gogny parameter sets D1S [24], D1N [25], and D1M [26] are used as the effective nucleon-nucleon interaction. D1N and D1M are newer parameter sets proposed in this decade and optimized for the description of the neutron matter equation of state (D1N) and neutron-rich nuclear matter (D1M). It is found that all of these parameter sets yield qualitatively the same results and quantitative differences are rather small. For example, the excitation energies of the linear-chain bands are within 1 MeV of each other. Therefore, in this paper, we report the results obtained by the D1S parameter set, because the threshold energies are most reasonably described by the D1S. The Coulomb interaction  $\hat{v}^C$  is approximated by a sum of seven Gaussians.  $\hat{t}_{c.m.}$  is the kinetic energy of the center of mass.

The AMD wave function  $\Phi_{\text{AMD}}$  is represented by a Slater determinant of single-particle wave packets,

$$\Phi_{\text{AMD}} = \mathcal{A}\{\varphi_1, \varphi_2, \dots, \varphi_A\} = \frac{1}{\sqrt{A!}} \det[\varphi_i(\mathbf{r}_j)], \quad (2)$$

where  $\varphi_i$  is the single-particle wave packet which is a direct product of the deformed Gaussian spatial part [27], spin ( $\chi_i$ ), and isospin ( $\xi_i$ ) parts,

$$\varphi_i(\mathbf{r}) = \phi_i(\mathbf{r}) \otimes \chi_i \otimes \xi_i, \quad (3)$$

$$\phi_i(\mathbf{r}) = \prod_{\sigma=x,y,z} \left( \frac{2\nu_\sigma}{\pi} \right)^{1/4} \exp \left\{ -\nu_\sigma \left( r_\sigma - \frac{Z_{i\sigma}}{\sqrt{\nu_\sigma}} \right)^2 \right\},$$

$$\chi_i = a_i \chi_\uparrow + b_i \chi_\downarrow, \quad \xi_i = \text{proton or neutron}. \quad (4)$$

The centroids of the Gaussian wave packets,  $\mathbf{Z}_i$ , the direction of nucleon spin,  $a_i, b_i$ , and the width parameter of the deformed Gaussian,  $\nu_\sigma$ , are the variables determined by the frictional cooling method explained below. Note that the AMD wave function (2) can be analytically decomposed into the internal wave function  $\Phi_{\text{int}}$  and the center-of-mass wave function  $\Phi_{c.m.}$ ,

$$\Phi_{\text{AMD}} = \Phi_{\text{int}} \Phi_{c.m.}, \quad (5)$$

$$\Phi_{c.m.} = \prod_{\sigma=x,y,z} \left( \frac{2A\nu_\sigma}{\pi} \right)^{1/4} \exp \{ -A\nu_\sigma R_\sigma^2 \}, \quad (6)$$

$$R_\sigma = \frac{1}{A} \sum_{i=1}^A r_{i\sigma}. \quad (7)$$

Therefore, the center-of-mass kinetic energy  $\hat{t}_{c.m.}$  is exactly removed and the model is free from the spurious motion. The intrinsic wave function is projected to the eigenstate of the parity to investigate both of the positive- and negative-parity states,

$$\Phi^\Pi = P^\Pi \Phi_{\text{int}} = \frac{1 + \Pi P_x}{2} \Phi_{\text{int}}, \quad \Pi = \pm, \quad (8)$$

where  $P^\Pi$  and  $P_x$  denote parity projector and operator. Using this wave function, the variational energy is defined as

$$E^\Pi = \frac{\langle \Phi^\Pi | H | \Phi^\Pi \rangle}{\langle \Phi^\Pi | \Phi^\Pi \rangle}. \quad (9)$$

By the frictional cooling method [28], the variables of the wave function ( $\mathbf{Z}_i, a_i, b_i, \nu_\sigma$ ) are determined so that  $E^\Pi$  is minimized. In this study, we add the constraint potential to the variational

energy,

$$\tilde{E}^\Pi = \frac{\langle \Phi^\Pi | H | \Phi^\Pi \rangle}{\langle \Phi^\Pi | \Phi^\Pi \rangle} + v_\beta (\langle \beta \rangle - \beta)^2 + v_\gamma (\langle \gamma \rangle - \gamma)^2, \quad (10)$$

where  $\langle \beta \rangle$  and  $\langle \gamma \rangle$  are the quadrupole deformation parameters of the intrinsic wave function defined in Refs. [5,29], with the  $v_\beta$  and  $v_\gamma$  parameters chosen to be large enough that  $\langle \beta \rangle$  and  $\langle \gamma \rangle$  are equal to  $\beta$  and  $\gamma$  after the variation. By minimizing  $\tilde{E}^\Pi$ , we obtain the optimized wave function  $\Phi^\Pi(\beta, \gamma) = P^\Pi \Phi_{\text{int}}(\beta, \gamma)$  which has the minimum energy for each set of  $\beta$  and  $\gamma$ . Note that our previous work employed only a  $\beta$  constraint, therefore the degree of freedom of  $\gamma$  deformation was not explicitly included.

After the variational calculation, the eigenstate of the total angular momentum  $J$  is projected out from  $\Phi^\Pi(\beta, \gamma)$ ,

$$\begin{aligned} \Phi_{MK}^{J\Pi}(\beta, \gamma) &= P_{MK}^J \Phi^\Pi(\beta, \gamma) \\ &= \frac{2J+1}{8\pi^2} \int d\Omega D_{MK}^{J*}(\Omega) \hat{R}(\Omega) \Phi^\Pi(\beta, \gamma). \end{aligned} \quad (11)$$

Here,  $P_{MK}^J$ ,  $D_{MK}^J(\Omega)$ , and  $\hat{R}(\Omega)$  are the angular-momentum projector, the Wigner  $D$  function, and the rotation operator, respectively. The integrals over Euler angles  $\Omega$  are evaluated numerically.

Next, we perform the generator coordinate method (GCM) calculation by employing the quadrupole deformation parameters  $\beta$  and  $\gamma$  as the generator coordinates. The wave function of GCM reads

$$\Psi_{Mn}^{J\Pi} = \sum_i \sum_K c_{Kin}^{J\Pi} \Phi_{MK}^{J\Pi}(\beta_i, \gamma_i), \quad (12)$$

where the unknown coefficients  $c_{Kin}^{J\Pi}$  and eigenenergies  $E_n^{J\Pi}$  are obtained by solving the Hill–Wheeler equation [30],

$$\begin{aligned} \sum_{i'K'} H_{KiK'i'}^{J\Pi} c_{K'i'n}^{J\Pi} &= E_n^{J\Pi} \sum_{i'K'} N_{KiK'i'}^{J\Pi} c_{K'i'n}^{J\Pi}, \\ H_{KiK'i'}^{J\Pi} &= \langle \Phi_{MK}^{J\Pi}(\beta_i, \gamma_i) | \hat{H} | \Phi_{MK'}^{J\Pi}(\beta_{i'}, \gamma_{i'}) \rangle, \\ N_{KiK'i'}^{J\Pi} &= \langle \Phi_{MK}^{J\Pi}(\beta_i, \gamma_i) | \Phi_{MK'}^{J\Pi}(\beta_{i'}, \gamma_{i'}) \rangle. \end{aligned} \quad (13)$$

We also calculate the overlap between  $\Psi_{Mn}^{J\Pi}$  and the basis wave function of the GCM  $\Phi_{MK}^{J\Pi}(\beta_i, \gamma_i)$ ,

$$|\langle \Phi_{MK}^{J\Pi}(\beta, \gamma) | \Psi_{Mn}^{J\Pi} \rangle|^2 / \langle \Phi_{MK}^{J\Pi}(\beta, \gamma) | \Phi_{MK}^{J\Pi}(\beta, \gamma) \rangle, \quad (14)$$

to discuss the dominant configuration in each state described by  $\Psi_{Mn}^{J\Pi}$ .

## B. Single-particle orbits

The neutron single-particle orbits of the intrinsic wave functions  $\Phi_{\text{int}}(\beta, \gamma)$  provide us the motion of the valence neutrons around the core nucleus. To construct a single-particle Hamiltonian, we first transform the single-particle wave packet  $\varphi_i$  to the orthonormalized basis,

$$\tilde{\varphi}_\alpha = \frac{1}{\sqrt{\lambda_\alpha}} \sum_{i=1}^A g_{i\alpha} \varphi_i. \quad (15)$$

Here,  $\lambda_\alpha$  and  $g_{i\alpha}$  are the eigenvalues and eigenvectors of the overlap matrix  $B_{ij} = \langle \varphi_i | \varphi_j \rangle$ . Using this basis, the Hartree–Fock single-particle Hamiltonian is derived,

$$h_{\alpha\beta} = \langle \tilde{\varphi}_\alpha | \hat{h} | \tilde{\varphi}_\beta \rangle + \sum_{\gamma=1}^A \langle \tilde{\varphi}_\alpha \tilde{\varphi}_\gamma | \hat{v}^N + \hat{v}^C | \tilde{\varphi}_\beta \tilde{\varphi}_\gamma - \tilde{\varphi}_\gamma \tilde{\varphi}_\beta \rangle + \frac{1}{2} \sum_{\gamma,\delta=1}^A \left\langle \tilde{\varphi}_\gamma \tilde{\varphi}_\delta \left| \tilde{\varphi}_\alpha^* \tilde{\varphi}_\beta \frac{\delta \hat{v}^N}{\delta \rho} \right| \tilde{\varphi}_\gamma \tilde{\varphi}_\delta - \tilde{\varphi}_\delta \tilde{\varphi}_\gamma \right\rangle. \quad (16)$$

The eigenvalues  $\epsilon_s$  and eigenvectors  $f_{\alpha s}$  of  $h_{\alpha\beta}$  give the single-particle energies and the single-particle orbits,  $\tilde{\phi}_s = \sum_{\alpha=1}^A f_{\alpha s} \tilde{\varphi}_\alpha$ . We calculate the amount of the positive-parity component in the single-particle orbit,

$$p^+ = \left| \left\langle \tilde{\phi}_s \left| \frac{1 + P_x}{2} \right| \tilde{\phi}_s \right\rangle \right|^2, \quad (17)$$

and angular momenta in the intrinsic frame,

$$j(j+1) = \langle \tilde{\phi}_s | \hat{j}^2 | \tilde{\phi}_s \rangle, \quad |j_z| = \sqrt{\langle \tilde{\phi}_s | \hat{j}_z^2 | \tilde{\phi}_s \rangle}, \quad (18)$$

$$l(l+1) = \langle \tilde{\phi}_s | \hat{l}^2 | \tilde{\phi}_s \rangle, \quad |l_z| = \sqrt{\langle \tilde{\phi}_s | \hat{l}_z^2 | \tilde{\phi}_s \rangle}, \quad (19)$$

which are used to discuss the properties of the single-particle orbits.

### C. Reduced width amplitude and decay width

Using the GCM wave function, we calculate the reduced width amplitudes (RWA)  $y_{lj_n^\pi}(r)$  for the  $\alpha + {}^{12}\text{Be}$  and  ${}^6\text{He} + {}^{10}\text{Be}$  decays, which are defined as

$$y_{lj_n^\pi}(r) = \sqrt{\frac{A!}{A_{\text{He}}! A_{\text{Be}}!}} \langle \phi_{\text{He}} [ \phi_{\text{Be}}(j_n^\pi) Y_{l0}(\hat{r}) ]_{JM} | \Psi_{Mn}^{J^\pi} \rangle, \quad (20)$$

where  $\phi_{\text{He}}$  denotes the ground-state wave function for  ${}^4\text{He}$  or  ${}^6\text{He}$ , and  $\phi_{\text{Be}}(j_n^\pi)$  denotes the wave functions for daughter nucleus  ${}^{12}\text{Be}$  or  ${}^{10}\text{Be}$  with spin-parity  $j_n^\pi$ .  $Y_{l0}(\hat{r})$  is the orbital angular momentum of the intercluster motion and is coupled with the angular momentum of  $\text{Be}(j_n^\pi)$  to yield the total spin-parity  $J^\pi$ .  $A_{\text{He}}$  and  $A_{\text{Be}}$  are the mass numbers of He and Be, respectively. The reduced width  $\gamma_{lj_n^\pi}$  is given by the square of the RWA,

$$\gamma_{lj_n^\pi}^2(a) = \frac{\hbar^2}{2\mu a} |a y_{lj_n^\pi}(a)|^2, \quad (21)$$

and the spectroscopic factor  $S$  is defined by the integral of the RWA,

$$S = \int_0^\infty r^2 |y_{lj_n^\pi}(r)|^2 dr. \quad (22)$$

The partial decay width is a product of the reduced width and the penetration factor  $P_l(a)$ ,

$$\Gamma_{lj_n^\pi} = 2P_l(a) \gamma_{lj_n^\pi}^2(a), \quad P_l(a) = \frac{ka}{F_l^2(ka) + G_l^2(ka)}, \quad (23)$$

where  $a$  denotes the channel radius, and  $P_l$  is given by the Coulomb regular and irregular wave functions  $F_l$  and  $G_l$ . The

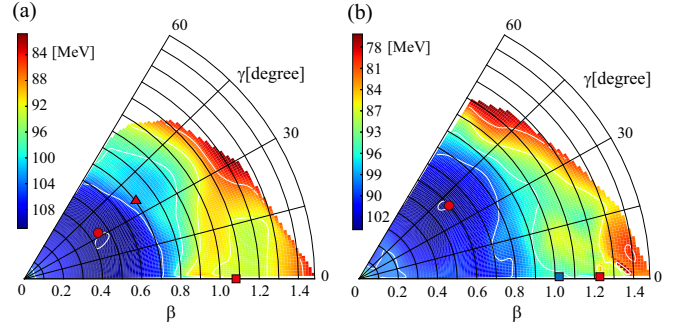


FIG. 1. The angular-momentum-projected energy surfaces for the (a)  $J^\pi = 0^+$  and (b)  $J^\pi = 1^-$  states as functions of quadrupole deformation parameters  $\beta$  and  $\gamma$ . The filled circles, triangles, and boxes in panel (a) show the ground, triangular, and linear-chain structures, while in panel (b) the circle shows the position of the energy minimum and filled boxes show the linear-chain configurations.

wave number  $k$  is determined by the decay  $Q$  value and the reduced mass  $\mu$  as  $k = \sqrt{2\mu E_Q}$ .

To calculate the RWA, we employ the Laplace expansion method given in Ref. [31]. This method is applicable to unequal-sized and deformed clusters without any approximation. The intrinsic wave functions for  ${}^{10,12}\text{Be}$  and  ${}^4,6\text{He}$  are generated by the AMD energy variation. For  ${}^{10}\text{Be}$ , we obtain two different intrinsic wave functions in which two valence neutrons occupy so-called  $\pi$  and  $\sigma$  orbits, respectively. We regard that the former correspond to the ground band (the  $0_1^+$  and  $2_1^+$  states), while the latter is the excited band (the  $0_2^+$  and  $2_3^+$  states). For  ${}^{12}\text{Be}$ , we obtain an intrinsic wave function in which two of four valence neutrons occupy  $\pi$  orbits and the others occupy  $\sigma$  orbits, which is regarded as the  ${}^{12}\text{Be}(0_1^+)$  and  ${}^{12}\text{Be}(2_1^+)$ . We also obtain another configuration having four valence neutrons in  $\pi$  orbits, which we regard as  ${}^{12}\text{Be}(0_2^+)$  and  ${}^{12}\text{Be}(2_2^+)$ . However, the decay width to these states are negligibly small, and so they are not discussed here. In the following calculation, we assume that the  ${}^4\text{He}$  and  ${}^6\text{He}$  clusters always have  $j^\pi = 0^+$ .

We also calculate the neutron spectroscopic factors in order to compare with the  $\alpha$ -cluster spectroscopic factors. The neutron spectroscopic factor  $S_n$  reads

$$S_n = \int_0^\infty r^2 |\varphi(r)|^2 dr, \quad (24)$$

where  $\varphi(r)$  is the overlap amplitude which is the overlap between the wave functions of nuclei with mass  $A$  and  $A+1$ ,

$$\varphi(r) = \sqrt{A+1} \langle \Psi_{M'n}^{J'^{\pi'}}({}^{15}\text{C}) | \Psi_{Mn}^{J^\pi}({}^{16}\text{C}) \rangle. \quad (25)$$

The intrinsic wave function for  ${}^{15}\text{C}$  is generated by the AMD energy variation. The spin-parity of  ${}^{15}\text{C}$  are chosen as  $J'^{\pi'} = 1/2^+$  (the ground state of  ${}^{15}\text{C}$ ) for positive-parity states of  ${}^{16}\text{C}$  and  $J'^{\pi'} = 1/2^-, 3/2^-, 5/2^-$  for negative-parity states.

## III. RESULTS AND DISCUSSION

### A. Energy surface and intrinsic structures

In Fig. 1, the energy surfaces for  $J^\pi = 0^+$  and  $J^\pi = 1^-$  states are shown as the function of quadrupole deformation

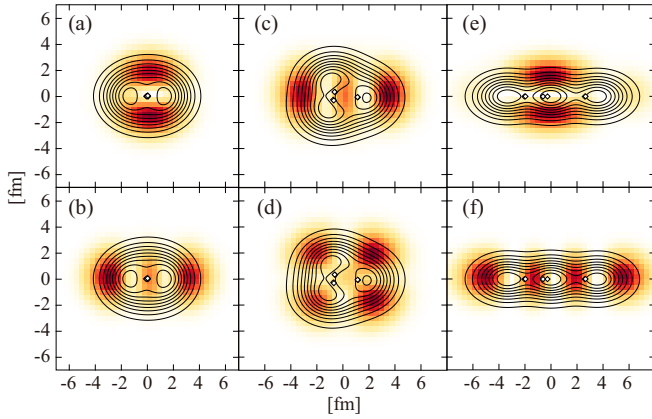


FIG. 2. The density distributions of positive-parity states of the (a), (b) ground, (c), (d) triangular, and (e), (f) linear-chain configurations. The contour lines show the proton density distributions. The color plots show the single-particle orbits occupied by four valence neutrons. The lower panels show the two most weakly bound neutrons, while the upper panels show the other two valence neutrons. Open boxes show the centroids of the Gaussian wave packets describing protons.

parameters  $\beta$  and  $\gamma$ . The circles on the energy surfaces show the position of the energy minima. First, we discuss three different structures on the energy surface of positive parity based on their intrinsic density distributions shown in Fig. 2. Although the  $\beta\gamma$ -constrained AMD method is newly applied in this study, these three structures are almost identical to those discussed in our previous work [22].

The energy minimum of the  $0^+$  state is located at  $(\beta, \gamma) = (0.45, 31^\circ)$  with the binding energy of 110.5 MeV. The intrinsic density distribution at the minimum is shown in Figs. 2(a) and 2(b). These figures clearly show that this structure has no outstanding clustering. Figures 2(c) and 2(d) show a different structure that we call the triangular configuration located around  $(\beta, \gamma) = (0.70, 37^\circ)$ . The  $3\alpha$  cluster core forms a triangle configuration, as seen in the density distribution. Table I rows (c) and (d) show that four valence neutrons occupy the  $(sd)^4$  shell, indicating  $2\hbar\omega$  excitation. However, due to its asymmetric shape, the valence proton orbits are an admixture of the positive- and negative-parity components. We note that a similar configuration appears in  $^{14}\text{C}$ , which also have

TABLE I. The properties of the valence neutron orbit shown in Fig. 2. Each column shows the single-particle energy  $\varepsilon$  in MeV, the amount of the positive-parity component  $p^+$  and the angular momenta defined by Eqs. (17)–(19).

	$\varepsilon$	$p^+$	$j$	$ j_z $	$l$	$ l_z $
(a)	-8.69	0.01	0.7	0.5	1.1	1.0
(b)	-3.95	0.99	2.2	0.5	1.8	0.4
(c)	-5.84	0.98	2.2	1.9	1.9	1.6
(d)	-2.97	0.98	2.4	1.9	2.1	1.8
(e)	-6.31	0.05	1.8	1.4	1.4	1.0
(f)	-3.16	0.07	2.8	0.6	2.6	0.3

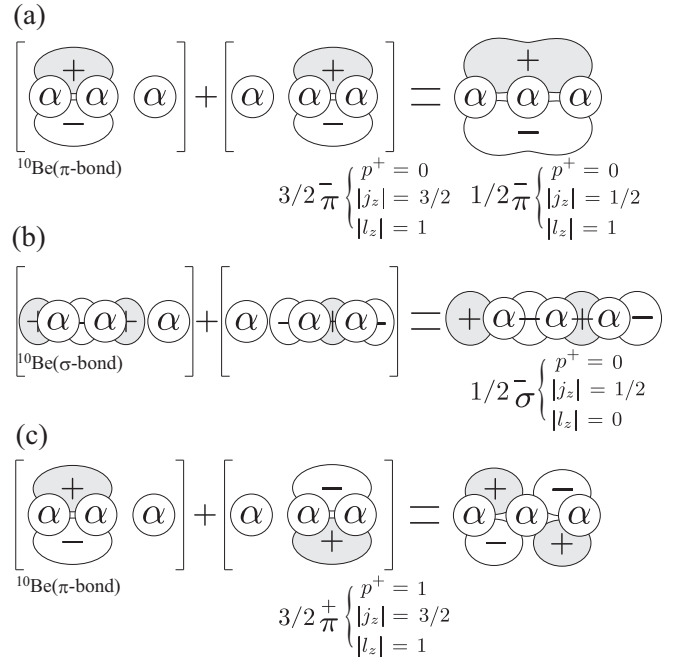


FIG. 3. The schematic figure showing the  $\pi$  and  $\sigma$  orbits around the linear chain. The combination of the  $\pi$  orbits around  $^{10}\text{Be}$  perpendicular to the symmetry axis generates  $\pi$  orbits, while the combination of parallel orbits around  $^{10}\text{Be}$  generates  $\sigma$  orbits.

valence neutrons shown in Fig. 2(c) but without those shown in Fig. 2(d).

A further increase of the deformation realizes the linear-chain configuration in the strongly prolate deformed region. In this region, there is an energy plateau around the local energy minimum located at  $(\beta, \gamma) = (1.08, 0^\circ)$ . As seen in Figs. 2(e) and 2(f), its proton density distribution shows striking  $3\alpha$  cluster configuration with linear alignment. In addition, the properties of valence neutron orbits listed in Table I rows (e) and (f) show that two valence neutrons occupy the so-called  $\pi$  orbit and the other two neutrons occupy the  $\sigma$  orbit. Here the  $\pi$  orbit in  $^{16}\text{C}$  is formed by the in-phase linear combination of the  $\pi$  orbit of  $^{10}\text{Be}$  and is denoted as  $3/2\pi^+$  and  $1/2\pi^-$  depending on the value of  $|j_z|$ , as illustrated in Fig. 3(a). The  $\sigma$  orbit is a linear combination of the  $\sigma$  orbit of  $^{10}\text{Be}$ , as illustrated in Fig. 3(b). Therefore, with these definitions, this state is regarded to have the  $(3/2\pi^-)^2(1/2\sigma^-)^2$  configuration.

The energy minimum of the energy surface for the  $1^-$  states [Fig. 1(b)] is located at  $(\beta, \gamma) = (0.59, 40^\circ)$  with the binding energy of 103.6 MeV. At the minimum, the single-particle properties show the  $1p1h$  configuration  $\nu(p_{1/2})^{-1}(d_{5/2})^1$ .

Figures 4(a)–4(d) show a basis wave function located at  $(\beta, \gamma) = (1.02, 1^\circ)$  in Fig. 1(b). This linear-chain configuration appears in the prolate deformed region, although there is no plateau in the energy surface of negative parity. The density distribution and properties of valence neutron orbits show that the  $3\alpha$  core is linearly aligned and three valence neutrons [Figs. 4(a)–4(c)] occupy  $(3/2\pi^-)^2(1/2\sigma^-)^1$  orbits similar to the linear-chain configuration of positive parity. However, the most weakly bound valence neutron [Fig. 4(d)] occupies a different orbit. The properties of single-particle orbit [Table II row (d)]

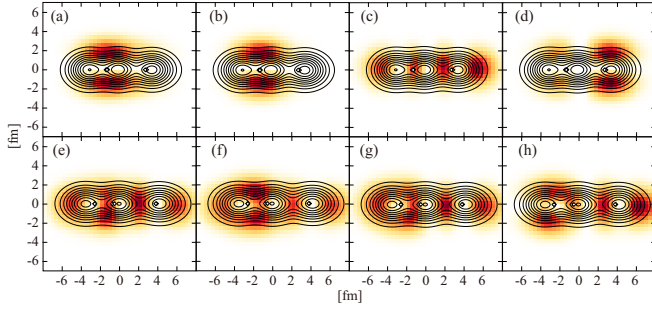


FIG. 4. The density distributions of negative-parity linear-chain states. Panels (a)–(d) correspond to the state at  $(\beta, \gamma) = (1.02, 1^\circ)$ , while panels (e)–(h) correspond to the state at  $(\beta, \gamma) = (1.23, 1^\circ)$ . The contour lines show the proton density distributions. The color plots show the single particle orbits occupied by four valence neutrons. Panels (a) and (e) show the most deeply bound valence neutrons, while panels (d) and (h) show the most weakly bound neutrons. Open boxes show the centroids of the Gaussian wave packets describing protons.

show that the most weakly bound valence neutron occupies the *ungerade*  $\pi$  orbit, which is a linear combination of the  ${}^{10}\text{Be}$   $\pi$  orbit with antiphase, as illustrated in Fig. 3(c). In addition, it can be seen that this  $(3/2_\pi^+)$  orbit locates around the  $\alpha$  particle of the right side, preferably. Note that this type of linear chain was not found in  ${}^{14}\text{C}$  [5,11]. We consider that this orbit is unbound in  ${}^{14}\text{C}$  and makes the negative-parity linear-chain unstable in  ${}^{14}\text{C}$ .

Figures 4(e)–4(h) show another intrinsic wave function belonging the linear-chain configuration that appears around  $(\beta, \gamma) = (1.23, 1^\circ)$ . Although the density distribution and properties of the valence neutron orbit do not show the clear molecular orbit nature because of the strong parity mixing, this intrinsic wave function has the largest overlap with member states of a linear-chain band, as mentioned in the next section.

### B. Excitation spectrum

Figure 5 shows the spectrum of the positive-parity states obtained by the GCM calculation. The properties of the several selected states are listed in Table III. For positive parity, it is found that three different bands exist: ground, triangular, and linear-chain bands. We classify the excited states which

TABLE II. Properties of the valence neutron orbits shown in Fig. 4. Each column shows the single-particle energy  $\varepsilon$  in MeV, the amount of positive-parity component  $p^+$  and the angular momenta defined by Eqs. (17)–(19).

	$\varepsilon$	$p^+$	$j$	$ j_z $	$l$	$ l_z $
(a)	−6.76	0.05	2.1	1.5	1.7	1.0
(b)	−6.63	0.16	2.0	1.5	1.7	1.0
(c)	−2.10	0.03	2.7	0.5	2.5	0.3
(d)	−0.78	0.92	3.0	1.5	2.7	1.0
(e)	−4.80	0.08	2.6	1.1	2.3	0.7
(f)	−4.48	0.16	2.7	1.2	2.4	0.8
(g)	−4.07	0.23	2.8	1.0	2.6	0.6
(h)	−2.23	0.57	3.0	1.2	2.8	0.8

TABLE III. Excitation energies (MeV),  $\alpha$  reduced widths ( $\text{MeV}^{1/2}$ ),  $\alpha$ -cluster and neutron spectroscopic factors of several selected positive-parity states. The reduced widths,  $\alpha$  and neutron  $S$  factors are calculated for the decays to the ground states of daughter nuclei.

Band	$J^\pi$	$E_x$	$\gamma_\alpha(6.0 \text{ fm})$	$S_\alpha$	$S_n$
Ground	$0_1^+$	0.00	0.00	0.03	0.22
	$2_1^+$	1.69	0.00	0.00	0.35
	$4_1^+$	4.04	0.00	0.00	0.01
Triangular	$0_2^+$	8.35	0.01	0.05	0.12
	$2_4^+$	10.22	0.00	0.00	0.01
	$2_5^+$	10.79	0.00	0.01	0.02
Linear chain	$0_6^+$	16.81	0.28	0.11	0.00
	$2_9^+$	17.51	0.23	0.07	0.00
	$4_{10}^+$	18.99	0.26	0.09	0.00
	$6_5^+$	21.49	0.23	0.07	0.00

have  $\alpha$  reduced widths larger than  $0.10 \text{ MeV}^{1/2}$  at the channel radius  $a = 6.0 \text{ fm}$  as cluster states. In these results, only the linear-chain band satisfies this condition. For the triangular configuration, the member states have overlap larger than 0.50 with the configuration shown in Figs. 2(c) and 2(d) are classified as the triangular band. The intraband  $B(E2)$  strengths are listed in Table IV.

The member states of the ground band are dominantly composed of the configurations around the energy minimum of the energy surface. The ground state has the largest overlap with the basis wave function shown in Figs. 2(a) and 2(b) that amounts to 0.98, and the calculated binding energy is 111.2 MeV which is close to the observed binding energy of 110.8 MeV. The excitation energies of other member states  $2_1^+$  and  $4_1^+$  are also reproduced. This band has no outstanding clustering but has a shell-model-like structure with a  $\nu(sd)^2$  configuration which can be confirmed from the small  $\alpha$  cluster spectroscopic factors and large neutron spectroscopic factors given in Table III.

Because of its triaxial deformed shape, the triangular configuration generates two rotational bands built on the  $0_2^+$  and  $2_5^+$

TABLE IV. Calculated in-band  $B(E2)$  strengths for the low-spin positive-parity states in units of  $e^2 \text{ fm}^4$ . The number in parentheses is the observed datum [32–36].

	$J_i \rightarrow J_f$	$B(E2; J_i \rightarrow J_f)$
Ground $\rightarrow$ ground	$2_1^+ \rightarrow 0_1^+$	6.7 (0.92 $\sim$ 4.2)
	$4_1^+ \rightarrow 2_1^+$	4.1
Triangular $\rightarrow$ triangular	$2_4^+ \rightarrow 0_2^+$	2.5
	$2_5^+ \rightarrow 0_2^+$	0.9
	$3_3^+ \rightarrow 2_4^+$	9.5
	$3_3^+ \rightarrow 2_5^+$	8.5
Linear chain $\rightarrow$ linear chain	$2_9^+ \rightarrow 0_6^+$	380.3
	$4_{10}^+ \rightarrow 2_9^+$	544.3
	$6_5^+ \rightarrow 4_{10}^+$	891.4

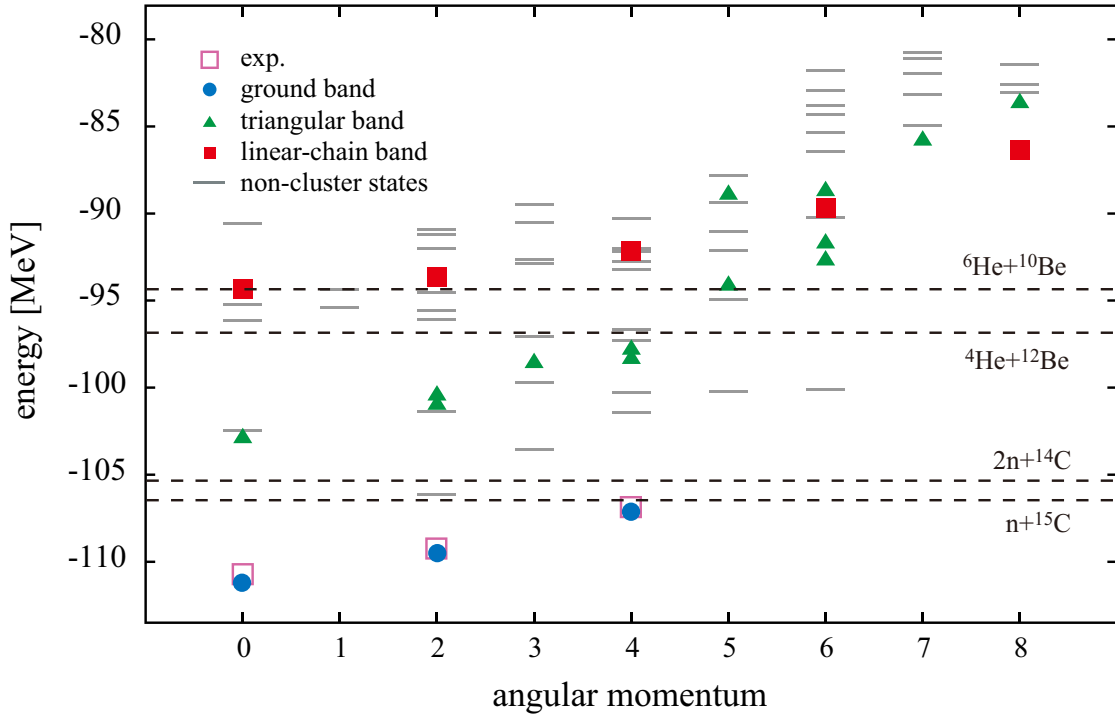


FIG. 5. The positive-parity energy levels up to  $J^\pi = 8^+$ . Open boxes show the observed states with the definite spin-parity assignments, and other symbols show the calculated result. The filled circles, triangles and boxes show the ground, triangular and linear-chain bands, while lines show the noncluster states which have reduced widths smaller than  $0.10 \text{ MeV}^{1/2}$  except for the triangular band.

states. The member states have overlap larger than 0.50 with the configuration shown in Figs. 2(c) and 2(d) which amount to, for example, 0.78 in the case of the  $0_2^+$  state. The member states with  $J^\pi \geq 5^+$  are fragmented into several states because of the coupling with the noncluster configurations. Compared to the linear-chain states, these bands have less pronounced clustering and  $\alpha$  clusters are considerably distorted. As a result, the member states gain binding energy and the low-spin states are located well below the cluster thresholds. Because of the  $\alpha$ -cluster distortion and deeper binding, the triangular configuration has small  $\alpha$  spectroscopic factors and reduced widths, as listed in Table III.

The linear-chain configuration generates a rotational band which is built on the  $0_6^+$  state located at 16.8 MeV. The bandhead  $0_6^+$  state has the largest overlap with the configuration shown in Figs. 2(e) and 2(f) that amounts to 0.94. The moment of inertia is estimated as  $\hbar/2\mathfrak{I} = 112 \text{ keV}$  which is considerably larger than those of the ground band ( $\hbar/2\mathfrak{I} = 196 \text{ keV}$ ) and triangular band ( $\hbar/2\mathfrak{I} = 238 \text{ keV}$ ). Owing to its large moment of inertia, the member state  $J^\pi = 8^+$  located at  $E_x = 24.8 \text{ MeV}$  becomes the yrast state. In addition, the large moment of inertia brings about the huge intraband  $B(E2)$  compared with those of the ground and triangular bands, as listed in Table IV. In contrast to the ground and triangular bands, the linear-chain band has the large  $\alpha$  cluster spectroscopic factors and very small neutron spectroscopic factors. As all member states locate above the  ${}^4\text{He} + {}^{12}\text{Be}$  and  ${}^6\text{He} + {}^{10}\text{Be}$  thresholds, the linear-chain states should decay into these two channels, which can be an important observable to identify the linear-chain state as discussed in the next section.

Figure 6 shows the spectrum of the negative-parity states. Only two states ( $2^-$  and  $5^-$ ), which are described by open boxes in the figure, were observed with the definite spin-parity assignments [19,37]. Our calculation shows the yrast band which is built on the  $2_1^-$  state located at 6.0 MeV, and the  $2_1^-$  and  $5_1^-$  member states of this rotational band are close to the observed two states. Since this band has the  $1p1h$  configuration  $\nu(p_{1/2})^{-1}(d_{5/2})^1$ , the spectroscopic factors in the  $[{}^{15}\text{C}(\text{g.s.}) \otimes j]$  channels are negligibly small but those in the  $[{}^{15}\text{C}(1/2^-) \otimes d_{5/2}]$ ,  $[{}^{15}\text{C}(3/2^-) \otimes d_{5/2}]$ , and  $[{}^{15}\text{C}(5/2^-) \otimes d_{5/2}]$  channels are large, as listed in Table V.

In the case of negative parity, the linear-chain configuration generates two different types of rotational bands. In the same manner as the positive-parity states, the excited states which have  $\alpha$  reduced widths larger than  $0.10 \text{ MeV}^{1/2}$  are classified as cluster states, and only linear-chain bands satisfy this condition. These bands are also located above the  ${}^4\text{He} + {}^{12}\text{Be}$  and  ${}^6\text{He} + {}^{10}\text{Be}$  thresholds. This is in contrast to  ${}^{14}\text{C}$  in which the linear-chain band is not obtained by the AMD

TABLE V. Neutron spectroscopic factors of yrast band for negative parity. The components of  ${}^{15}\text{C} \otimes s_{1/2}$  and  ${}^{15}\text{C} \otimes d_{3/2}$  are negligibly small.

	$2_1^-$	$3_1^-$	$4_1^-$	$5_1^-$
${}^{15}\text{C}(1/2^-) \otimes d_{5/2}$	0.03	0.42		
${}^{15}\text{C}(3/2^-) \otimes d_{5/2}$	0.34	0.04	0.19	
${}^{15}\text{C}(5/2^-) \otimes d_{5/2}$	0.67	0.07	0.48	0.27

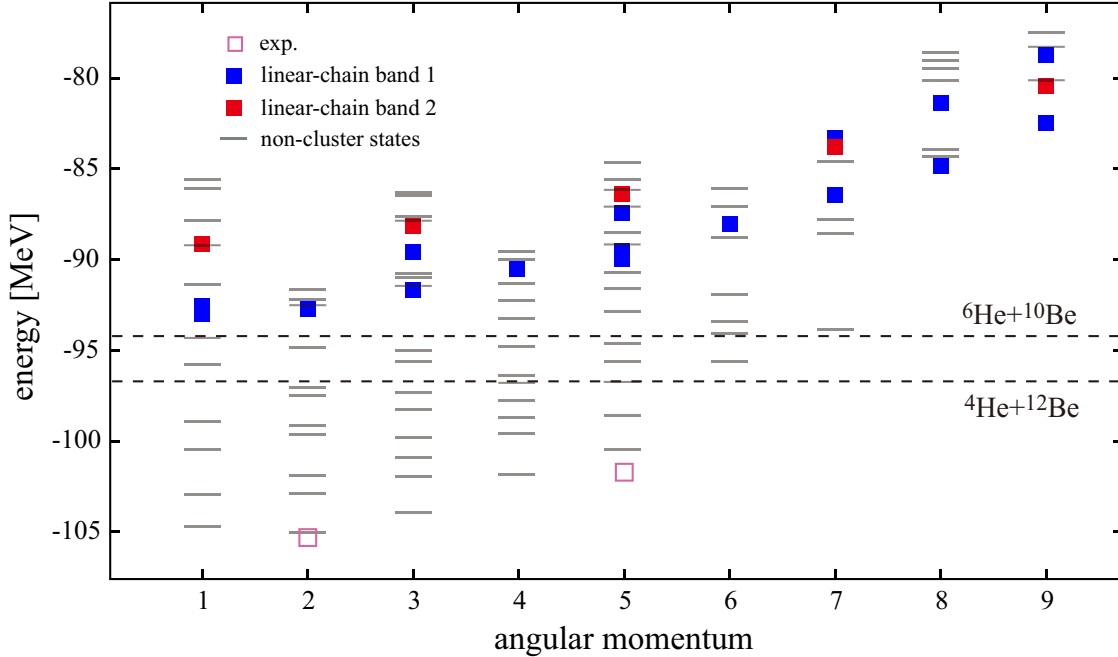


FIG. 6. Negative-parity energy levels up to  $J^\pi = 9^-$ . Open boxes show the observed states with the definite spin-parity assignments [19,37], and other symbols show the calculated result. The filled boxes show the linear-chain bands, while lines show the noncluster states which have the reduced widths less than  $0.10 \text{ MeV}^{1/2}$ .

calculations [5,11,15]. The properties of the several selected linear-chain states are listed in Table VI and the  $B(E2)$  strengths are listed in Table VII.

The first band, which we call linear-chain band 1 (blue square), is dominantly composed of the wave function shown in Figs. 4(a)–4(d) although it is mixed with noncluster configurations. Furthermore, there is a mixing of  $K = 0^-$  and  $1^-$  components. As a result, the member states of this band are fragmented into several states. For example, we classify both of the  $1_7^-$  and  $1_8^-$  states as the member states of the band, whose overlaps with the basis wave functions shown in Figs. 4(a)–4(d) are 0.24 and 0.64, respectively. Because of the fragmentation,

TABLE VI. Excitation energies (MeV),  $\alpha$  reduced widths ( $\text{MeV}^{1/2}$ ), and  $\alpha$ -cluster spectroscopic factors of several selected states for negative parity.  $\gamma_\alpha$  and  $S_\alpha$  show the decay to the ground state ( $0_1^+$ ) of  ${}^{12}\text{Be}$ .

Band	$J^\pi$	$E_x$	$\gamma_\alpha(5.5 \text{ fm})$	$\gamma_\alpha(7.0 \text{ fm})$	$S_\alpha$
yrast band	$2_1^-$	6.11			
	$3_1^-$	7.25	0.00	0.00	0.02
	$4_1^-$	9.34			
	$5_1^-$	10.71	0.00	0.00	0.00
Linear chain band 1	$1_7^-$	18.28	0.04	0.00	0.01
	$1_8^-$	18.64	0.02	0.01	0.00
	$3_9^-$	19.45	0.10	0.01	0.03
	$3_{13}^-$	21.57	0.05	0.02	0.01
Linear chain band 2	$1_{11}^-$	22.05	0.04	0.12	0.03
	$3_{14}^-$	23.00	0.04	0.12	0.03
	$5_{15}^-$	24.76	0.03	0.11	0.02
	$7_6^+$	27.35	0.06	0.11	0.01

the intraband  $B(E2)$  values are smaller than those of positive-parity linear-chain band. However, the moment of inertia,  $\hbar/2\mathfrak{I} = 118 \text{ keV}$ , is comparable with that of positive-parity linear chain. In this band, the neutron spectroscopic factors are negligible. Compared with the positive-parity linear chain,  $\alpha$  spectroscopic factors are small, but sufficiently larger than other negative-parity states.

The other band, the linear-chain band 2 (red squares), is built on the  $1_{11}^-$  state at  $E_x = 22.1 \text{ MeV}$  which is about 3.6 MeV higher than the linear-chain band 1. The  $1_{11}^-$  state has the largest overlap with the wave function shown in Figs. 4(e)–4(h), which amounts to 0.92. In contrast with the linear-chain band 1, the member states of this band have the  $K = 0$  quantum number and clearly form a single rotational band. In addition, the moment of inertia,  $\hbar/2\mathfrak{I} = 98 \text{ keV}$ , and the intraband  $B(E2)$  values are as large as those of positive-parity linear-chain band. As well as the linear-chain band 1, the neutron spectroscopic

TABLE VII. The calculated in-band  $B(E2)$  strengths for the low-spin negative-parity states in units of  $e^2 \text{ fm}^4$ .

	$J_i \rightarrow J_f$	$B(E2; J_i \rightarrow J_f)$
Linear chain band 1	$2_9^- \rightarrow 1_7^-$	53.2
	$2_9^- \rightarrow 1_8^-$	25.0
	$3_9^- \rightarrow 2_9^-$	37.7
	$3_{13}^- \rightarrow 2_9^-$	0.1
	$4_{11}^- \rightarrow 3_9^-$	72.0
	$4_{11}^- \rightarrow 3_{13}^-$	4.0
Linear chain band 2	$3_{14}^- \rightarrow 1_{11}^-$	492.2
	$5_{15}^- \rightarrow 3_{14}^-$	561.6
	$7_6^- \rightarrow 5_{15}^-$	556.1

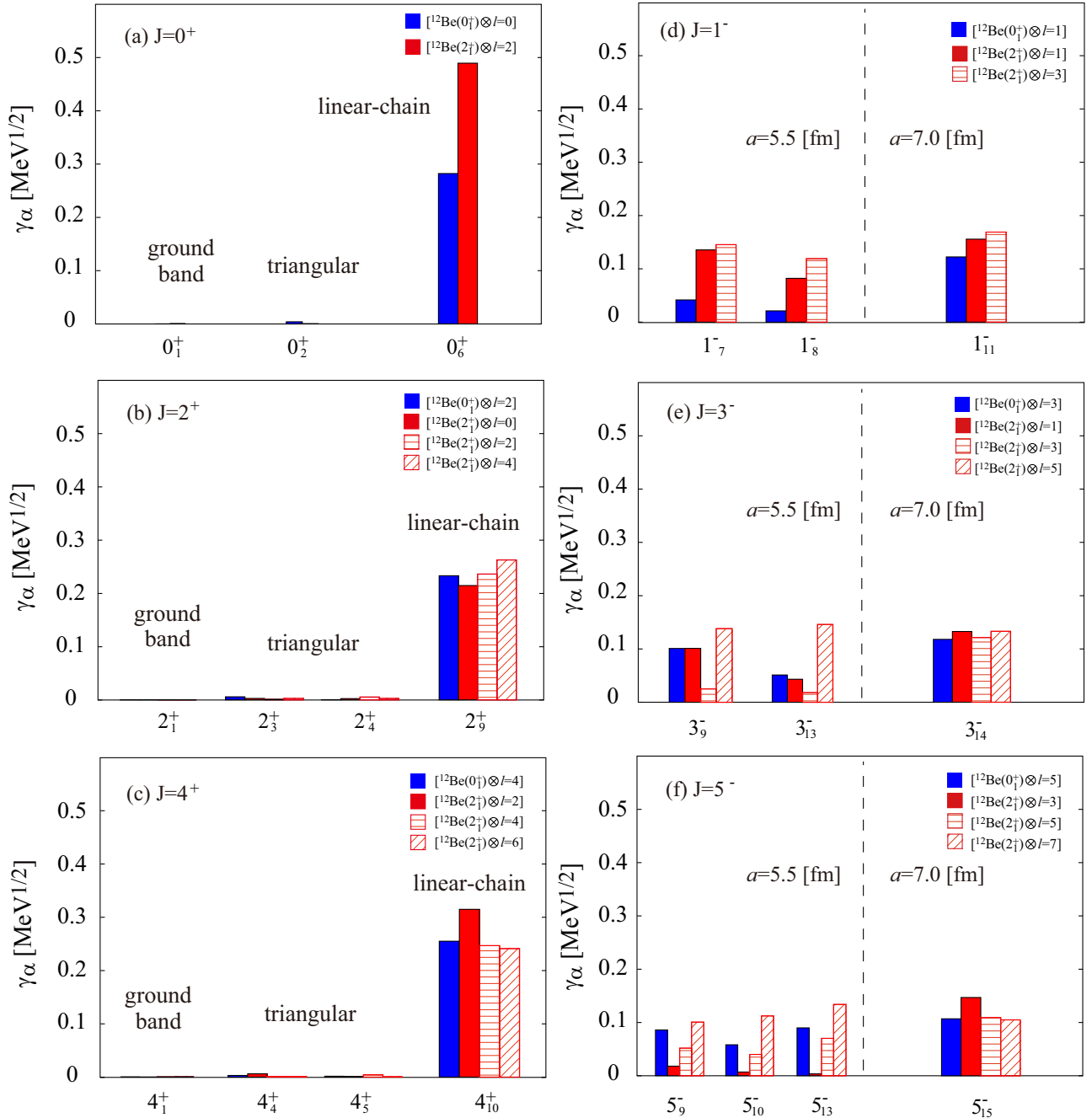


FIG. 7. Calculated  $\alpha$ -decay reduced widths. Panels (a)–(c) show the decay of the positive-parity states to the ground band of  $^{12}\text{Be}$ . Panels (d)–(f) show the decay of the negative-parity states to the ground band of  $^{12}\text{Be}$ . The channel radii  $a$  are 6.0 fm for panels (a)–(c) and 5.5 (left side), 7.0 (right side) fm for panels (d)–(f), respectively.

factors are negligible while the  $\alpha$  spectroscopic factors are a bit larger but smaller than those of the positive-parity linear-chain band.

### C. Decay mode

Figure 7 shows the  $\alpha$  reduced widths of several selected low-spin states. For positive parity, we show the member states of the ground, triangular, and linear-chain bands, while for negative parity, we show only the states which have reduced widths larger than  $0.1 \text{ MeV}^{1/2}$ . The decay channels are indicated as  $[^{12}\text{Be}(j^\pi) \otimes l]$  where  $j^\pi$  and  $l$  denote the angular

momentum of the  $^{12}\text{Be}$  ground band and the relative angular momentum between  $^{12}\text{Be}$  and  $\alpha$  particles, respectively. Here,  $^{12}\text{Be}$  is assumed to have two neutrons in a  $\pi$  orbit and the other two neutrons in a  $\sigma$  orbit. The channel radii  $a$  are 6.0 fm for Figs. 7(a)–7(c) and 5.5 (left side), 7.0 (right side) fm for Figs. 7(d)–7(f), which are chosen to be smoothly connected to the Coulomb wave function. The detailed values of  $\alpha$  and  $^6\text{He}$  decay widths for linear-chain states are listed in Table VIII.

In positive parity, the linear-chain band (the  $0_6^+$ ,  $2_9^+$ , and  $4_{10}^+$  states) has large reduced widths compared with the ground and triangular bands. Note also that the  $\alpha$  reduced widths of other

TABLE VIII. Partial decay widths (keV) of linear-chain bands for (a) positive-parity and (b) negative-parity linear-chain band 2. The channel radii  $a$  are (a) 6.0 fm and (b) 7.0 fm.

$J^\pi$	$E_x$	(a) Positive parity			
		$\Gamma_\alpha({}^{12}\text{Be}(0_1^+))$	$\Gamma_\alpha({}^{12}\text{Be}(2_1^+))$	$\Gamma_{6\text{He}}({}^{10}\text{Be}(0_1^+))$	$\Gamma_{6\text{He}}({}^{10}\text{Be}(2_1^+))$
$0_6^+$	16.81	335	1		
$2_9^+$	17.51	300	118	0	
$4_{10}^+$	18.99	505	954	33	
$6_5^+$	21.49	535	1591	78	18
(b) Negative parity					
$1_{11}^-$	22.05	198	567	77	63
$3_{14}^-$	23.00	196	597	84	115
$5_{15}^-$	24.76	181	615	92	173
$7_6^-$	27.35	224	763	100	225

excited states are also much smaller than the linear-chain band. Hence, in the calculated energy region, the linear chain band has the largest reduced widths. Another point to be noted is the decay pattern of the linear-chain band. The reduced widths in the  $[{}^{12}\text{Be}(2_1^+) \otimes l]$  channels are as large as or even larger than those in the  $[{}^{12}\text{Be}(0_1^+) \otimes l]$  channel. This dominance of the  ${}^{12}\text{Be}(2_1^+)$  component in the linear-chain band is owed to the strong angular correlation between  $\alpha$  clusters which is brought about by their linear alignment. This property is in contrast to the Hoyle state where  $\alpha$  particles are mutually orbiting with  $l = 0$  and, hence, the  ${}^8\text{Be}(0_1^+)$  component dominates [38]. Similar properties of the linear-chain configuration was also discussed in  ${}^{12}\text{C}$  [39] and  ${}^{14}\text{C}$  [11]. Therefore, if the decay to  ${}^{12}\text{Be}(2_1^+)$  is confirmed, it will provide strong evidence for the linear-chain formation.

Figure 8 shows the  ${}^6\text{He}$  reduced widths of linear-chain states for positive parity. We calculated the  ${}^6\text{He}$  reduced widths for both the  ${}^6\text{He} + {}^{10}\text{Be}(0_1^+, 2_1^+)$  and  ${}^6\text{He} + {}^{10}\text{Be}(0_2^+, 2_3^+)$  channels. Here we assumed that the ground band of  ${}^{10}\text{Be}(0_1^+ \text{ and } 2_1^+)$  has the  $\pi$ -orbit neutrons, while the excited state ( $0_2^+, 2_3^+$ , and so on) of  ${}^{10}\text{Be}$  has the  $\sigma$ -orbit neutrons. Figure 8(a) corresponds to the decay to  ${}^6\text{He} + {}^{10}\text{Be}(0_1^+, 2_1^+)$  and the Fig. 8(b) corresponds to the decay to  ${}^6\text{He} + {}^{10}\text{Be}(0_2^+, 2_3^+)$ . Although the magnitudes

of the  ${}^6\text{He}$  reduced widths are about a factor of two smaller than that of  $\alpha$  reduced widths, they are still sufficiently large compared with any other excited states. It is also noted that the magnitudes of  ${}^6\text{He} + {}^{10}\text{Be}(0_1^+, 2_1^+)$  and  ${}^6\text{He} + {}^{10}\text{Be}(0_2^+, 2_3^+)$  reduced widths are almost of the same order. This is caused by the unique configuration of linear-chain state in  ${}^{16}\text{C}$ . The linear-chain configuration in  ${}^{16}\text{C}$  has the two  $\pi$ -orbit neutrons and two  $\sigma$ -orbit neutrons, so the linear-chain configuration of  ${}^{16}\text{C}$  can decay into both  ${}^{10}\text{Be}(0_1^+, 2_1^+)$  and  ${}^{10}\text{Be}(0_2^+, 2_3^+)$ . The results shown in Fig. 8 are consistent with this explanation. This decay property should be compared with that of the linear chains in  ${}^{14}\text{C}$ . As already discussed in our previous paper [11], the  $\pi$ -bond linear-chain state of  ${}^{14}\text{C}$  dominantly decays into  ${}^{10}\text{Be}(0_1^+, 2_1^+)$ , while the decay to  ${}^{10}\text{Be}(0_2^+, 2_3^+)$  is suppressed. In contrast to the  $\pi$ -bond linear chain, the  $\sigma$ -bond linear-chain state of  ${}^{14}\text{C}$  dominantly decays into  ${}^{10}\text{Be}(0_2^+, 2_3^+)$  and the decay to  ${}^{10}\text{Be}(0_1^+, 2_1^+)$  is suppressed.

For the negative parity, it can be seen that the linear-chain bands 1 and 2 show relatively smaller reduced widths compared with the positive-parity linear-chain band. The linear-chain configurations of negative parity do not match the  ${}^4\text{He} + {}^{12}\text{Be}(0_1^+, 2_1^+)$  configuration due to the existence of the valence neutron which occupies the *ungerade*  $\pi_{3/2}^+$

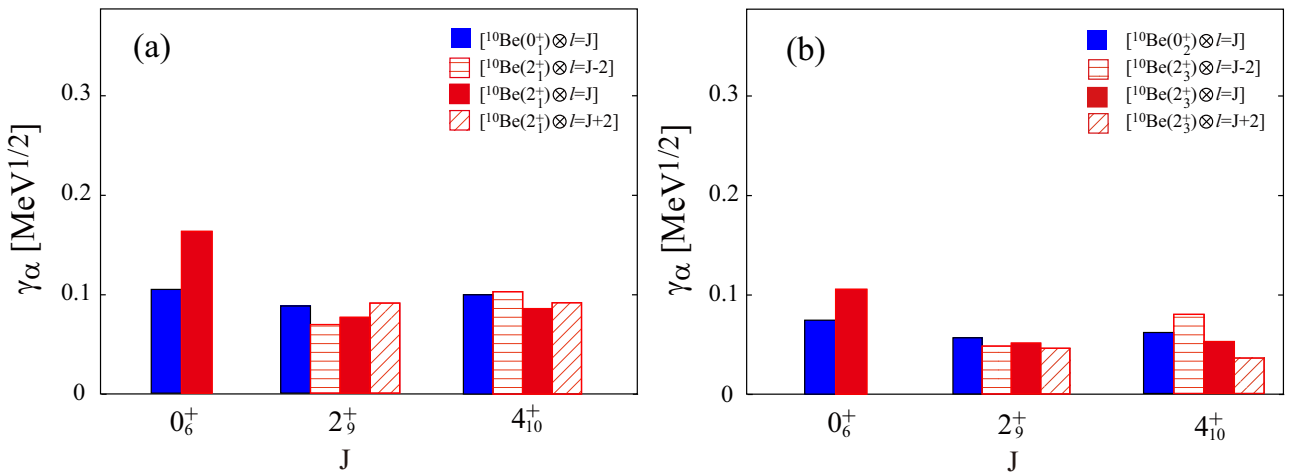


FIG. 8. The calculated  ${}^6\text{He}$ -decay reduced widths of linear-chain states in positive parity. In panel (a), the decay to the ground band of  ${}^{10}\text{Be}$  is shown. In panel (b), the decay to the excited band of  ${}^{10}\text{Be}$  is shown. The channel radius  $a$  is 6.0 fm.

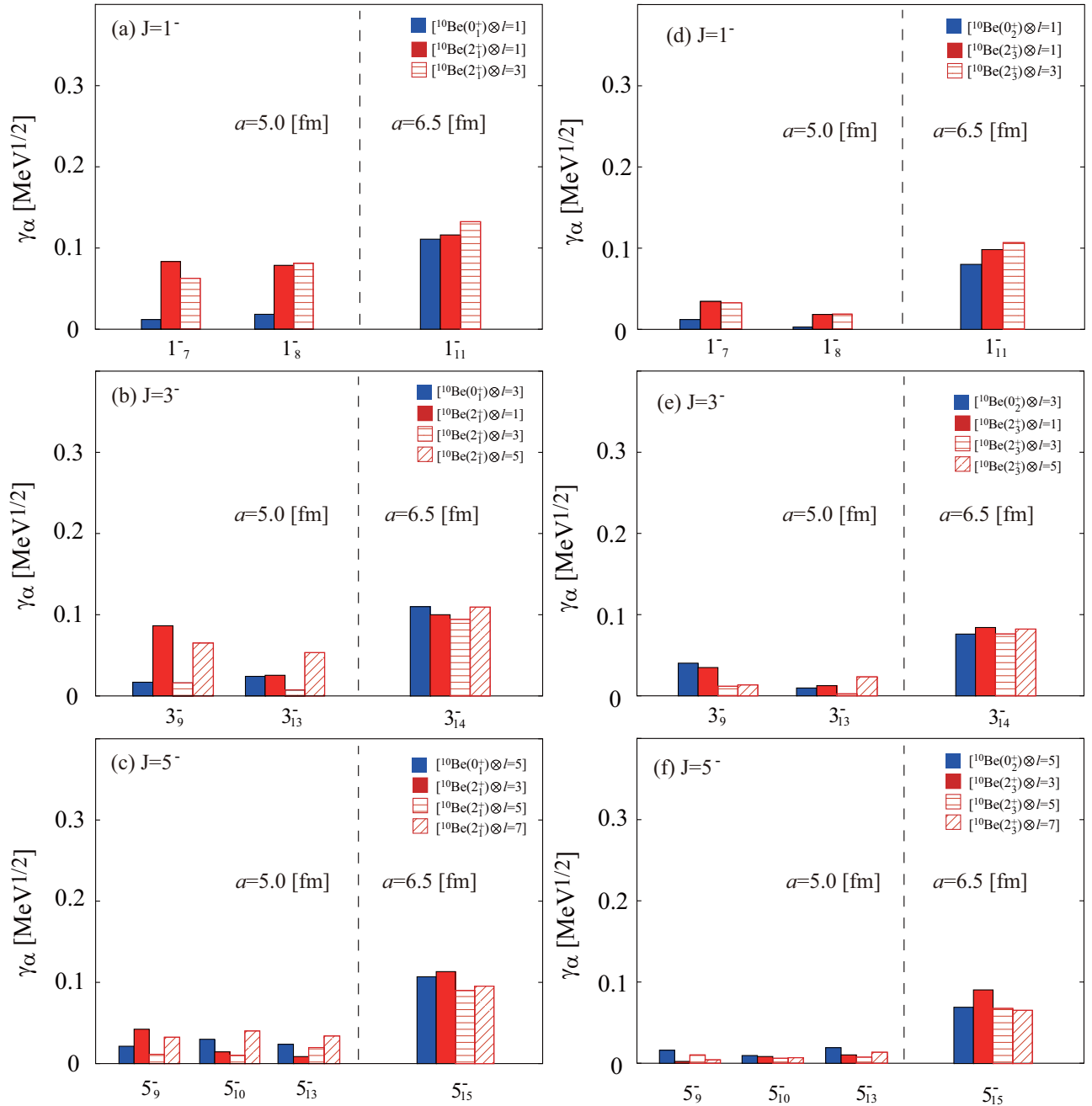


FIG. 9. The calculated  ${}^6\text{He}$ -decay reduced widths of linear-chain states in negative parity. Panels (a)–(c) show the decay to the ground band of  ${}^{10}\text{Be}$ . Panels (d)–(f) show the decay to the excited band of  ${}^{10}\text{Be}$ .

(see Fig. 4). Therefore, the decay to the  ${}^4\text{He} + {}^{12}\text{Be}(0_1^+, 2_1^+)$  channel is suppressed. The characteristic decay patterns of the linear-chain configuration can also be seen in negative parity; namely, the reduced widths in the  $[{}^{12}\text{Be}(2_1^+) \otimes l]$  channels are larger than in the  $[{}^{12}\text{Be}(0_1^+) \otimes l]$  channels. In addition, the partial decay widths of the linear-chain band 2 listed in Table VIII (b) are very large because of their high excitation energies. Therefore, if it is observed, the linear-chain formation in the negative-parity can be supported strongly. However, it is not easy to distinguish the linear-chain band 1 and 2 from  $\alpha$  reduced widths because they are almost of the same magnitude.

Figure 9 shows the  ${}^6\text{He}$  reduced widths of negative-parity linear-chain states for both the  ${}^{10}\text{Be}(0_1^+, 2_1^+)$  and  ${}^{10}\text{Be}(0_2^+, 2_3^+)$  channels. It is interesting that a characteristic difference between the linear-chain bands 1 and 2 appears in the  ${}^6\text{He}$  reduced widths. The linear-chain band 2 has the same magnitude of the  ${}^6\text{He}$  reduced widths as the  $\alpha$  reduced widths. In addition, the  ${}^6\text{He}$  reduced widths of the linear-chain band 2 are even larger than those of positive-parity linear-chain band (see Fig. 8). On the other hand, the linear-chain band 1 has the smaller  ${}^6\text{He}$  reduced widths, especially as it rarely decays into  ${}^6\text{He} + {}^{10}\text{Be}(0_2^+, 2_3^+)$ . This characteristic difference enables us to distinguish the linear-chain bands 1 and 2.

A high-lying excited state at 20.6 MeV was observed by the breakup of  ${}^6\text{He} + {}^{10}\text{Be}$  [23]. Since the spin-parity was not assigned, several calculated excited states can be the candidate of the observed high-lying state, including the linear-chain states naturally. However, the positive- or negative-parity linear-chain states only show the large  ${}^6\text{He}$  reduced widths near 20.6 MeV. Although further experimental studies are needed, we suggest the linear-chain state as the candidate for the observed high-lying state.

#### IV. SUMMARY

We discussed the properties of the linear-chain states of  ${}^{16}\text{C}$  based on the AMD. In particular, we focused on their decay modes to allow for experimental identification.

In positive parity, it is shown that the linear-chain configuration has the valence neutrons occupying molecular orbits  $(3/2_{\pi}^{-})^2(1/2_{\sigma}^{-})^2$ . It generates a rotational band built on the  $0^+$  state at 16.8 MeV and its moment of inertia is estimated as  $\hbar/2\mathfrak{I} = 112$  keV. It is shown that the linear-chain states have the large  $\alpha$  and  ${}^6\text{He}$  reduced widths. In particular, the large  $\alpha$  reduced widths in the  $\alpha + {}^{12}\text{Be}(2_1^+)$  channel is strong evidence for the linear-chain configuration. In the case of the  ${}^6\text{He}$  decay, the magnitudes of the reduced decay widths in both  ${}^{10}\text{Be}(0_1^+, 2_1^+)$  and  ${}^{10}\text{Be}(0_2^+, 2_3^+)$  channels are almost of the same order. Compared with  ${}^{14}\text{C}$ , this is caused by the unique configuration of linear-chain state in  ${}^{16}\text{C}$ .

In the negative-parity states, it is found that two types of linear-chain bands exist. The first band, which we call the linear-chain band 1, is composed of the linear-chain configuration with the  $(3/2_{\pi}^{-})^2(1/2_{\sigma}^{-})(3/2_{\pi}^+)$  molecular orbits. This band is built on  $1^-$  states located around 18.5 MeV. Because of the mixing with noncluster states and the mixing of  $K = 0^-$  and  $1^-$  components, the member states are fragmented into several states. The other band, which we call the linear-chain band 2, is built on  $1^-$  states located around 22.1 MeV. Although this band does not have the clear molecular-orbit configuration, the single rotational  $K = 0$  band is clearly formed with the large moment of inertia  $\hbar/2\mathfrak{I} = 98$  keV. The  $\alpha$  reduced widths of these two linear chains are smaller than those of the positive-parity linear-chain band, but are sufficiently large to be distinguished from other noncluster states. These two linear-chains cannot be distinguished based on the  $\alpha$  reduced widths because they are almost same magnitude. However, the  ${}^6\text{He}$  reduced widths of the linear-chain band 2 are larger than those of linear-chain band 1. We conclude that this characteristic difference enables us to distinguish the linear-chain bands 1 and 2.

#### ACKNOWLEDGMENTS

T.B. acknowledges the support by JSPS KAKENHI Grant No. JP16J04889. M.K. acknowledges the support by the Grants-in-Aid for Scientific Research on Innovative Areas from MEXT (Grant No. 2404:24105008) and JSPS KAKENHI Grant No. JP16K05339.

- 
- [1] N. Soic *et al.*, *Phys. Rev. C* **68**, 014321 (2003).  
 [2] M. Milin *et al.*, *Nucl. Phys. A* **730**, 285 (2004).  
 [3] D. L. Price, M. Freer, N. I. Ashwood, N. M. Clarke, N. Curtis, L. Giot, V. Lima, P. McEwan, B. Novatski, N. A. Orr, S. Sakuta, J. A. Scarpaci, D. Stepanov, and V. Ziman, *Phys. Rev. C* **75**, 014305 (2007).  
 [4] P. J. Haigh, N. I. Ashwood, T. Bloxham, N. Curtis, M. Freer, P. McEwan, D. Price, V. Ziman, H. G. Bohlen, T. Kokalova, C. Schulz, R. Torabi, W. vonOertzen, C. Wheldon, W. Catford, C. Harlin, R. Kalpakchieva, and T. N. Massey, *Phys. Rev. C* **78**, 014319 (2008).  
 [5] T. Suhara and Y. Kanada-En'yo, *Phys. Rev. C* **82**, 044301 (2010).  
 [6] T. Suhara and Y. Kanada-En'yo, *Phys. Rev. C* **84**, 024328 (2011).  
 [7] M. Freer, J. D. Malcolm, N. L. Achouri, N. I. Ashwood, D. W. Bardayan, S. M. Brown, W. N. Catford, K. A. Chipps, J. Cizewski, N. Curtis, K. L. Jones, T. Munoz-Britton, S. D. Pain, N. Soic, C. Wheldon, G. L. Wilson, and V. A. Ziman, *Phys. Rev. C* **90**, 054324 (2014).  
 [8] J.-P. Ebran, E. Khan, T. Niksic, and D. Vretenar, *Phys. Rev. C* **90**, 054329 (2014).  
 [9] A. Fritsch, S. Beceiro-Novo, D. Suzuki, W. Mittig, J. J. Kolata, T. Ahn, D. Bazin, F. D. Becchetti, B. Bucher, Z. Chajecki, X. Fang, M. Febraro, A. M. Howard, Y. Kanada-Enyo, W. G. Lynch, A. J. Mitchell, M. Ojaruega, A. M. Rogers, A. Shore, T. Suhara, X. D. Tang, R. Torres-Isea, and H. Wang, *Phys. Rev. C* **93**, 014321 (2016).  
 [10] Z. Y. Tian *et al.*, *Chin. Phys. C* **40**, 111001 (2016).  
 [11] T. Baba and M. Kimura, *Phys. Rev. C* **94**, 044303 (2016).  
 [12] Y. Yoshida and Y. Kanada-En'yo, *Prog. Theor. Exp. Phys.* **2016**, 123D04 (2016).  
 [13] H. Yamaguchi *et al.*, *Phys. Lett. B* **766**, 11 (2017).  
 [14] J. Li, Y. L. Ye, Z. H. Li, C. J. Lin, Q. T. Li, Y. C. Ge, J. L. Lou, Z. Y. Tian, W. Jiang, Z. H. Yang, J. Feng, P. J. Li, J. Chen, Q. Liu, H. L. Zang, B. Yang, Y. Zhang, Z. Q. Chen, Y. Liu, X. H. Sun, J. Ma, H. M. Jia, X. X. Xu, L. Yang, N. R. Ma, and L. J. Sun, *Phys. Rev. C* **95**, 021303 (2017).  
 [15] T. Baba and M. Kimura, *Phys. Rev. C* **95**, 064318 (2017).  
 [16] J.-P. Ebran, E. Khan, T. Niksic, and D. Vretenar, *J. Phys. G* **44**, 103001 (2017).  
 [17] N. Itagaki, S. Okabe, K. Ikeda, and I. Tanihata, *Phys. Rev. C* **64**, 014301 (2001).  
 [18] B. J. Greenhalgh, B. R. Fulton, D. L. Watson, N. M. Clarke, L. Donadille, M. Freer, P. J. Leask, W. N. Catford, K. L. Jones, and D. Mahboub, *Phys. Rev. C* **66**, 027302 (2002).  
 [19] H. G. Bohlen *et al.*, *Phys. Rev. C* **68**, 054606 (2003).  
 [20] N. I. Ashwood *et al.*, *Phys. Rev. C* **70**, 064607 (2004).  
 [21] J. Maruhn, N. Loebl, N. Itagaki, and M. Kimura, *Nucl. Phys. A* **833**, 1 (2010).  
 [22] T. Baba, Y. Chiba, and M. Kimura, *Phys. Rev. C* **90**, 064319 (2014).  
 [23] D. Dell'Aquila, I. Lombardo, L. Acosta, R. Andolina, L. Auditore, G. Cardella, M. B. Chatterjee, E. DeFilippo, L. Francalanza, B. Gnoffo, G. Lanzalone, A. Pagano, E. V. Pagano, M. Papa, S. Pirrone, G. Politi, F. Porto, L. Quattrocchi, F. Rizzo, E. Rosato, P. Russotto, A. Trifiro, M. Trimarchi, G. Verde, and M. Vigilante, *Phys. Rev. C* **93**, 024611 (2016).

- [24] J. F. Berger, M. Girod, and D. Gogny, *Comput. Phys. Commun.* **63**, 365 (1991).
- [25] F. Chappert, M. Girod, and S. Hilaire, *Phys. Lett. B* **668**, 420 (2008).
- [26] S. Goriely, S. Hilaire, M. Girod, and S. Peru, *Phys. Rev. Lett.* **102**, 242501 (2009).
- [27] M. Kimura, *Phys. Rev. C* **69**, 044319 (2004).
- [28] Y. Kanada-En'yo and H. Horiuchi, *Prog. Theor. Phys.* **93**, 115 (1995).
- [29] M. Kimura, R. Yoshida, and M. Isaka, *Prog. Theor. Phys.* **127**, 287 (2012).
- [30] D. L. Hill and J. A. Wheeler, *Phys. Rev.* **89**, 1102 (1953).
- [31] Y. Chiba and M. Kimura, *Prog. Theor. Exp. Phys.* **2017**, 053D01 (2017).
- [32] N. Imai, H. J. Ong, N. Aoi, H. Sakurai, K. Demichi, H. Kawasaki, H. Baba, Z. Dombradi, Z. Elekes, N. Fukuda, Z. Fulop, A. Gelberg, T. Gomi, H. Hasegawa, K. Ishikawa, H. Iwasaki, E. Kaneko, S. Kanno, T. Kishida, Y. Kondo, T. Kubo, K. Kurita, S. Michimasa, T. Minemura, M. Miura, T. Motobayashi, T. Nakamura, M. Notani, T. K. Onishi, A. Saito, S. Shimoura, T. Sugimoto, M. K. Suzuki, E. Takeshita, S. Takeuchi, M. Tamaki, K. Yamada, K. Yoneda, H. Watanabe, and M. Ishihara, *Phys. Rev. Lett.* **92**, 062501 (2004).
- [33] H. J. Ong, N. Imai, N. Aoi, H. Sakurai, Z. Dombradi, A. Saito, Z. Elekes, H. Baba, K. Demichi, Z. S. Fulop, J. Gibelin, T. Gomi, H. Hasegawa, M. Ishihara, H. Iwasaki, S. Kanno, S. Kawai, T. Kubo, K. Kurita, Y. U. Matsuyama, S. Michimasa, T. Minemura, T. Motobayashi, M. Notani, S. Ota, H. K. Sakai, S. Shimoura, E. Takeshita, S. Takeuchi, M. Tamaki, Y. Togano, K. Yamada, Y. Yanagisawa, and K. Yoneda, *Phys. Rev. C* **73**, 024610 (2006).
- [34] H. J. Ong, N. Imai, D. Suzuki, H. Iwasaki, H. Sakurai, T. K. Onishi, M. K. Suzuki, S. Ota, S. Takeuchi, T. Nakao, Y. Togano, Y. Kondo, N. Aoi, H. Baba, S. Bishop, Y. Ichikawa, M. Ishihara, T. Kubo, K. Kurita, T. Motobayashi, T. Nakamura, T. Okumura, and Y. Yanagisawa, *Phys. Rev. C* **78**, 014308 (2008).
- [35] M. Wiedeking *et al.*, *Phys. Rev. Lett.* **100**, 152501 (2008).
- [36] M. Petri *et al.*, *Phys. Rev. C* **86**, 044329 (2012).
- [37] Y. Satou *et al.*, *Phys. Lett. B* **728**, 462 (2014).
- [38] Y. Funaki, H. Horiuchi, and A. Tohsaki, *Prog. Part. Nucl. Phys.* **82**, 78 (2015).
- [39] Y. Suzuki, H. Horiuchi, and K. Ikeda, *Prog. Theor. Phys.* **47**, 1517 (1972).